

# Inferring Hidden Symmetries of Exotic Magnets from Learning Explicit Order Parameters

Nihal Rao,<sup>1, 2</sup> Ke Liu,<sup>1, 2, \*</sup> and Lode Pollet<sup>1, 2, 3</sup>

<sup>1</sup> Arnold Sommerfeld Center for Theoretical Physics,

University of Munich, Theresienstr. 37, 80333 München, Germany

<sup>2</sup>Munich Center for Quantum Science and Technology (MCQST), Schellingstr. 4, 80799 München, Germany

<sup>3</sup>Wilczek Quantum Center, School of Physics and Astronomy,

Shanghai Jiao Tong University, Shanghai 200240, China

(Dated: June 2, 2022)

An exotic magnet may be mapped onto a simple ferromagnet by the existence of a high-symmetry point. Knowledge of conventional ferromagnetic systems may then be carried over to provide insight into intricate orders. Here we demonstrate how an unsupervised and interpretable machine-learning approach can efficiently search for potential high-symmetry points in unconventional magnetic phases via learning analytical order parameters. The method is applied to the Heisenberg-Kitaev model on a honeycomb lattice, where we identify a  $D_2$  and  $D_{2h}$  order and their hidden  $O(3)$  symmetry. Moreover, we elucidate that the pictorial zigzag and stripy patterns only partially capture the magnetization of exotic order in the Heisenberg-Kitaev model. The complete magnetization curves are given by the  $D_2$  and  $D_{2h}$  ordering matrices, which are also the transformations manifesting the hidden symmetries. Our work highlights the significance of explicit order parameters to many-body spin systems and the property of interpretability for the physical application of machine-learning techniques.

## I. INTRODUCTION

Applications of machine learning in different fields of physics have become ubiquitous and witnessed a dramatic rise in the past few years [1], ranging from statistical physics [2, 3], condensed matter physics [4–6], chemistry and material science [7–9], to high energy physics [10–12] and quantum computation [13–15]. Although studies in the earlier stages have primarily focused on benchmarking relatively simple models, many recent developments are moving towards practical tools for solving more complicated and challenging problems. Instances of these advances include, for example, discovering new classes of wavefunctions in strongly-correlated systems [16], improving the accuracy on atoms and small molecules [17, 18], designing efficient algorithms [19–21], and analyzing experiments [22–24].

Here we explore the potential of using machine-learning techniques to search for hidden symmetries in many-body spin systems. Symmetry is at the heart of our understanding of physics. Apparent symmetries such as time, spatial, and rotational invariance lead to the conservation of energy, momentum, and angular momentum, respectively. However, quite often, the effective symmetry of a system is not apparent, which we refer to as hidden symmetry. For instance, in some extended Kitaev systems, which are subject to active research due to their proximity to Kitaev spin liquids [25] and other exotic phases [26–30], there exist high-symmetry points. At these points, an exotic phase may be transformed to a simple ferromagnet [31–33]. Knowledge of conventional orders can then be carried over, and Goldstone

modes may be realized even when the Hamiltonian seemingly manifests a low discrete symmetry. Others remarkable examples are the Bethe-ansatz solvable  $SU(3)$  point in the spin-1 bilinear-biquadratic chain [34–37] and the emergent  $O(4)$  symmetry in the spin-1/2  $J$ - $Q$  model [38].

Although hidden symmetries are of broad relevance and rich in physics, identifying them is highly non-trivial and very much problem-dependent, usually requiring remarkable insight. Therefore, it would be interesting and desired if machine learning can facilitate their identification.

In this paper, we show that the tensorial-kernel support vector machine (TK-SVM) [39–41], which is an *unsupervised* and *interpretable* machine-learning method, provides an efficient and versatile approach to detect hidden symmetries in exotic magnets. We demonstrate the method by applying it to the honeycomb Heisenberg-Kitaev (HK) model, where our machine correctly identifies the hidden  $O(3)$  points in the exotic phases therein and the associated transformations. Moreover, we clarify that the pictorial description of the zigzag and stripy orders only partially reflect the exotic magnetic order in the HK model. The complete orders are characterized by the  $D_2$  and  $D_{2h}$  ordering matrices.

The paper is organized as follows. In Section II we define the HK Hamiltonian and provide a non-technical introduction to TK-SVM. Section III discusses the machine-learned phase diagram. Section IV is devoted to explicit order parameters and the corresponding magnetization curves. The connection between hidden symmetries and ordering matrices is given in Section V. We conclude in Section VI with an outlook.

\* ke.liu@lmu.de

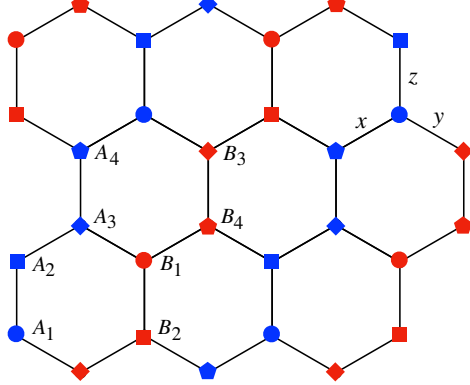


FIG. 1. Depiction of the magnetic structure of exotic orders in the honeycomb Heisenberg-Kitaev model Eq. (1). The magnetic cell contains two sectors marked by  $A$  (blue) and  $B$  (red), while the minimal translational unit consists of eight spins.  $x, y, z$  label the three distinct bonds in the Kitaev interaction.

## II. MODEL AND METHOD

We consider the HK model on a honeycomb lattice to demonstrate the concept. It should be noted however that, the following discussion is intended to provide a general guidance for using TK-SVM to search for exotic orders and hidden symmetries, and is transferable to other spin systems.

### A. Heisenberg-Kitaev Hamiltonian

The honeycomb HK model is defined as

$$H = \sum_{\langle ij \rangle \gamma} J \vec{S}_i \cdot \vec{S}_j + K S_i^\gamma S_j^\gamma, \quad (1)$$

where  $J$  and  $K$  denote the Heisenberg and Kitaev interaction, respectively, and can be parameterized by an angle variable  $\varphi \in [0, 2\pi]$  with  $K = \sin \varphi$ ,  $J = \cos \varphi$ ;  $\gamma \in \{x, y, z\}$  labels the three types of nearest-neighboring bonds  $\langle ij \rangle_\gamma$ , as depicted in Figure 1.

The Hamiltonian Eq. (1) is known to capture some of the key physics of the Kitaev materials [26–29] and plays host of two exotic magnetic orders and two Kitaev spin liquids (KSLs) [29, 32].

### B. TK-SVM

The TK-SVM is an interpretable and unsupervised approach to detect general symmetry-breaking spin orders [39, 40] and emergent local constraints [41, 42]. It is formulated in terms of the decision function

$$d(\mathbf{x}) = \sum_{\mu\nu} C_{\mu\nu} \phi_\mu(\mathbf{x}) \phi_\nu(\mathbf{x}) - \rho. \quad (2)$$

Here,  $\mathbf{x} = \{S_i^a | a = x, y, z; i = 1, 2, \dots, N\}$  denotes configurations of  $N$  spins and serves as training data.  $\phi_\mu(\mathbf{x})$  maps  $\mathbf{x}$  to a tensorial feature space, the  $\phi$ -space, which can represent general spin orders, regardless of exotic magnets, tensorial nematics [39, 40] and emergent local constraints for spin liquids [41, 42].  $C_{\mu\nu}$  can be viewed as an encoder of order parameters, from which explicit expressions of the detected orders are identified.  $\rho$  is a bias parameter probing whether two sample sets originate from the same phase. See Appendix A for details.

Although the decision function Eq. (2) carries out a binary classification between two sets of data, TK-SVM can also classify multiple data sets. Such a multi-classification is essentially realized by individual binary problems but makes it possible to compute a phase diagram via unsupervised graph partitioning.

Consider a spin Hamiltonian characterized by a number of physical parameters, such as temperature and different kinds of interactions. We can cover its parameters space,  $\mathcal{V}$ , by a grid of the same dimensionality. The choice of the grid is arbitrary, either uniform or distorted to have denser nodes in the most interesting subregions of  $\mathcal{V}$ . We collect spin configurations  $\mathbf{x}$  at vertices of the grid and perform the SVM multi-classification on the sampled data. For a grid of  $M$  vertices, this will produce  $M(M-1)/2$  decision functions as Eq. (2), comprising of binary classifications between each pair of vertices. We then introduce a weighted edge between two vertices, and the weight,  $w(\rho) \in [0, 1]$ , is based on the bias parameter in the corresponding  $d(x)$ . In this way, we create a graph with  $M$  vertices and  $M(M-1)/2$  edges; its partitioning will give the phase diagram.

In formal terms, the graph can be described by a  $M$ -by- $M$  Laplacian matrix  $\hat{L}$ . The off-diagonal entries of  $\hat{L}$  accommodate edge weights connecting vertices, and the diagonal entries are degrees of those vertices. The partitioning can be solved by Fiedler's theory of spectral clustering [43, 44],

$$\hat{L}\mathbf{f}_i = \lambda_i \mathbf{f}_i. \quad (3)$$

The second smallest eigenvalue  $\lambda_2$  measures the algebraic connectivity of the graph. The corresponding eigenvector  $\mathbf{f}_2$  is referred as the *Fiedler vector*, which reflects how the vertices are clustered and plays the role of a phase diagram in the context of TK-SVM [40, 41]. Cf. Appendix B for details.

## III. MACHINE-LEARNED PHASE DIAGRAM

A typical application of TK-SVM consists of two steps: (i) detecting the topology of the phase diagram, (ii) extracting and verifying order parameters. We focus here on the phase diagram of the HK model Eq. (1), and save the discussion of order parameters for the next section.

To this purpose, we introduce a fictitious grid that spans uniformly in the space of  $\varphi$ , with a spacing of  $\delta\varphi = \frac{\pi}{48}$ . At each  $\varphi$ , we collect 500 spin configurations

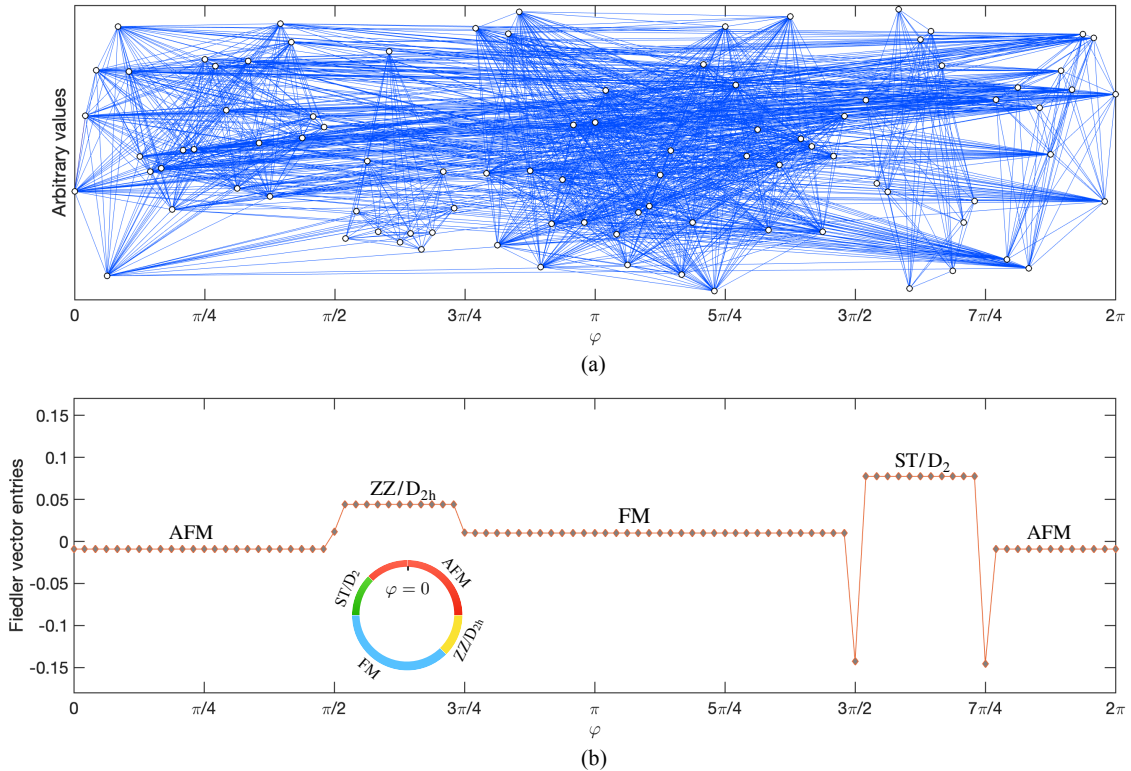


FIG. 2. Machine-learned phase diagram. (a) A fully-connected graph of 96 vertices (white cycles) and 4,560 edges (blue lines). Each vertex represents a value of  $\varphi$ . The edges are weighted according to biases  $\rho$  learned in a rank-1 TK-SVM multi-classification (cf. Section III and Appendix B for details). Since the parameter space is one-dimensional, a second dimension is introduced with arbitrary values to avoid collapse of edges. (b) The Fiedler vector obtained from partitioning the graph. Each entry corresponds to a vertex, while gradients in their value reflect the clustering of the graph. The plateaus indicate stable phases, and the sudden jumps signal phase transitions. The phases are interpreted in Section IV and are labelled following the common convention: AFM, antiferromagnet; ZZ, zigzag; FM, ferromagnet; ST, stripy. In addition, the ST and ZZ region are also marked according to the  $D_2$  and  $D_{2h}$  magnetizations measured in Figure 3. All phases and their transitions are discriminated by a single unsupervised partitioning. The inner panel shows a circular representation of the phase diagram.

at a low temperature  $T = 10^{-3}\sqrt{J^2 + K^2}$ . The samples are prepared by classical parallel tempering Monte Carlo (PTMC) simulations on a lattice of 10,368 spins ( $72 \times 72$  honeycomb unit cells). Next, we perform TK-SVM with different ranks over these data. However, it turns out that a rank-1 TK-SVM (cf. Appendix A), which detects magnetic orders, is sufficient to learn the phase diagram. The result is a graph of 96 vertices and 4,560 edges as shown in Figure 2a.

The Fiedler vector obtained from partitioning the graph is depicted in Figure 2b (see also Appendix B). Each of its entry represents to a vertex of the grid, hence a  $\varphi$ . The values of Fiedler vector entries for those  $\varphi$ 's that are classified into the same subgraph component will be identical or very close, while those falling into different subgraphs will display considerable contrast.

Evidently, the Fiedler vector shows four subgraph components, indicating four stable phases. This in fact reproduces the classical HK phase diagram [45]. The four plateaus respectively correspond to the antiferromagnetic (AFM), zigzag (ZZ), ferromagnetic (FM) and stripy (ST)

phase, following the labeling in Figure 2b. However, as we shall discuss in Section IV, the regions  $\varphi \in (\frac{\pi}{2}, \frac{3\pi}{4})$  and  $(\frac{3\pi}{2}, \frac{7\pi}{4})$  may be more suitably referred as  $D_2$  and  $D_{2h}$  orders.

Sudden jumps in the Fiedler vector entries manifest phase transitions, which are seen to occur at  $J = 0, K = \pm 1$  ( $\varphi = \frac{\pi}{2}, \frac{3\pi}{2}$ ) and  $J = -K$  ( $\varphi = \frac{3\pi}{4}, \frac{7\pi}{4}$ ). The boundaries at  $K = \pm 1$  correspond to the Kitaev limits. Different from the cases of quantum spin-1/2 and spin-1, where KSLs are proposed to extend to finite regions of  $J$  [32, 46–49], in the large- $S$  limit, KSLs are unstable against the Heisenberg interaction and reduce to critical points. Nevertheless, this will not affect our discussion on the hidden symmetries in the HK model.

We note that the learning of Figure 2 is unsupervised. No prior knowledge of the phase diagram and order parameters were used. Moreover, all the four phases are discriminated simultaneously by a *single* partitioning. This is in sharp contrast with conventional calculations of a phase diagram, which would scan the phases and their transitions individually.

Phases	Ordering Matrices			
Stripy	$T_{1,2}^{A,B} = \begin{pmatrix} 1 & 0 & 0 \\ 0 & 1 & 0 \\ 0 & 0 & 1 \end{pmatrix}$ , $T_{3,4}^{A,B} = \begin{pmatrix} -1 & 0 & 0 \\ 0 & -1 & 0 \\ 0 & 0 & -1 \end{pmatrix}$			
Zigzag	$T_{1,4}^A, T_{2,3}^B = \begin{pmatrix} 1 & 0 & 0 \\ 0 & 1 & 0 \\ 0 & 0 & 1 \end{pmatrix}$ , $T_{2,3}^A, T_{1,4}^B = \begin{pmatrix} -1 & 0 & 0 \\ 0 & -1 & 0 \\ 0 & 0 & -1 \end{pmatrix}$			
$D_2$	$T_1^{A,B} = \begin{pmatrix} 1 & 0 & 0 \\ 0 & 1 & 0 \\ 0 & 0 & 1 \end{pmatrix}$ , $T_2^{A,B} = \begin{pmatrix} -1 & 0 & 0 \\ 0 & 0 & 1 \\ 0 & 1 & 0 \end{pmatrix}$ , $T_3^{A,B} = \begin{pmatrix} -1 & 0 & 0 \\ 0 & 1 & 0 \\ 0 & 0 & -1 \end{pmatrix}$ , $T_4^{A,B} = \begin{pmatrix} 1 & 0 & 0 \\ 0 & -1 & 0 \\ 0 & 0 & -1 \end{pmatrix}$			
$D_{2h}$	$T_1^{A,B} = \pm \begin{pmatrix} 1 & 0 & 0 \\ 0 & 1 & 0 \\ 0 & 0 & 1 \end{pmatrix}$ , $T_2^{A,B} = \pm \begin{pmatrix} 1 & 0 & 0 \\ 0 & 1 & 0 \\ 0 & 0 & -1 \end{pmatrix}$ , $T_3^{A,B} = \pm \begin{pmatrix} -1 & 0 & 0 \\ 0 & 1 & 0 \\ 0 & 0 & -1 \end{pmatrix}$ , $T_4^{A,B} = \pm \begin{pmatrix} -1 & 0 & 0 \\ 0 & 1 & 0 \\ 0 & 0 & 1 \end{pmatrix}$			

TABLE I. Ordering matrices for the stripy, zigzag,  $D_2$  and  $D_{2h}$  orders. The four orders share the same magnetic cell, which consists of two sectors, dubbed  $A, B$ , and in total eight spins as shown in Figure 1. The stripy and zigzag orders define patterns of staggered spins (Figure 4) and can be expressed by the identity and inversion matrices, where a sign difference acts on all three spin components. The  $D_2$  and  $D_{2h}$  orders involve four and eight distinct matrices, respectively, forming the respective three-dimensional dihedral groups. Their ordering matrices also define the sublattice transformation for the hidden  $O(3)$  symmetries in the Heisenberg-Kitaev model.

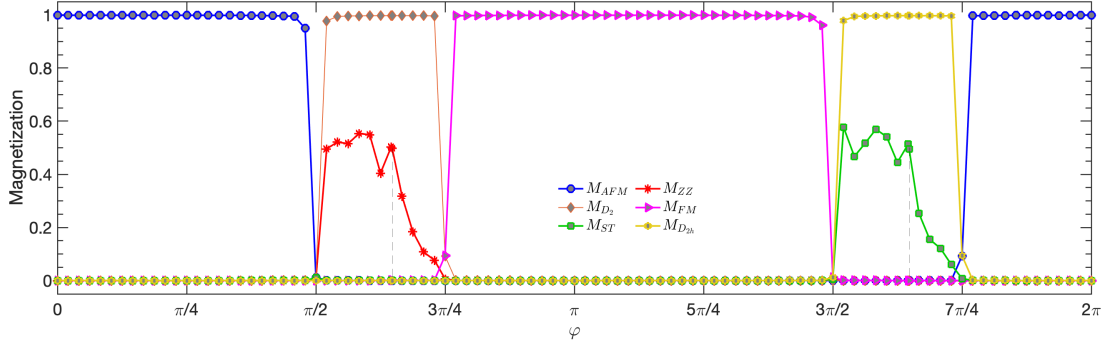


FIG. 3. Measurements of order parameters. The FM, AFM,  $D_2$  and  $D_{2h}$  magnetization are measured as a function of  $\varphi$  at low temperature  $T = 10^{-3}\sqrt{J^2 + K^2}$ . In each phase, the respective magnetization saturates to unity ( $|M| = 1$ ), while others vanish. In addition, the stripy (ST) and zigzag (ZZ) order illustrated in Figure 4 are measured for comparison. Although they also develop a finite magnitude in the regions  $\varphi \in (\frac{\pi}{2}, \frac{3\pi}{4})$  and  $(\frac{3\pi}{2}, \frac{7\pi}{4})$ , they appear to only partially reflect the ordering. The dashed lines mark the hidden  $O(3)$  points, where  $K = -2J$  and  $|M| = 0.5$  for the ST and ZZ order.

#### IV. EXPLICIT ORDER PARAMETERS

We move on to understand the nature of the phases. In virtue of the strong interpretability of TK-SVM, we are able to extract the analytical order parameter for each phase in Fig. 2 from the  $C_{\mu\nu}$  matrix in the decision function. As the FM and AFM order are trivial, we will focus on the two exotic states.

The interpreted order parameters of the  $D_2$  and  $D_{2h}$  phase can be expressed as (cf. Appendix A for details)

$$\vec{M} = \frac{1}{8} \sum_{A,B} \sum_{k=1}^4 T_k^{A,B} \vec{S}_k, \quad (4)$$

where  $T_k^{A,B}$  are ordering matrices tabulated in Table I, and  $A, B$  denote the two sublattice sectors indicated in Figure 1. (Note that the numeration of spins in the  $A$  and  $B$  sector are different.)

Both orders consist of eight sublattices. The  $D_2$  order is formulated by four different matrices with  $T_k^A = T_k^B$ ,

forming the three-dimensional dihedral group  $D_2$ . These matrices have been proposed in the study of orbital degeneracy of Mott insulators [50, 51] and are used to identify the hidden symmetries of the HK model [27, 31], which will be discussed in Section V. The  $D_{2h}$  order can be viewed as an AFM version of the  $D_2$  order, where  $T_k^A = -T_k^B$  in the respective sublattice. It is thereby named after the dihedral group  $D_{2h} \cong D_2 \times Z_2$ .

These order parameters, as well as those for the FM and AFM phase, are measured at  $T = 10^{-3}\sqrt{J^2 + K^2}$  as the temperature in the training. As shown in Figure 3, the respective magnetization saturates to unity and firmly extends in each phase, and vanishes in other phases. This validates our interpretation of those phases.

Special mention is warranted to the regions  $\varphi \in (\frac{\pi}{2}, \frac{3\pi}{4})$  and  $(\frac{3\pi}{2}, \frac{7\pi}{4})$  which are usually referred as zigzag and stripy phases, whose representative patterns are illustrated in Figure 4 and formulated in Table I. Measurement of these phases in Figure 3 suggests that, although the zigzag and stripy order develop a finite magnitude,

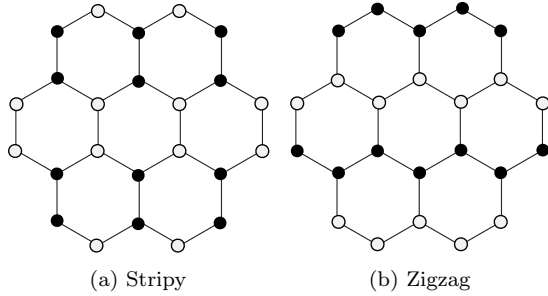


FIG. 4. Depiction of a stripy and zigzag order. Black ( $\vec{S}$ ) and white ( $-\vec{S}$ ) cycles denote opposite spins, where  $\vec{S}$  may point to arbitrary direction. The corresponding ordering matrices are given in Table I, and their magnitudes in the Heisenberg-Kitaev model are measured in Figure 3.

they are not seen to satisfactorily reflect the full ordering. The associated magnetizations appear to fluctuate around  $|M| \sim 0.5$  near the Kitaev limits  $\varphi = \frac{\pi}{2}, \frac{3\pi}{2}$ , then experience a rapid decay after passing  $\varphi = \arctan(-2)$ , which are the hidden  $O(3)$  points in the HK Hamiltonian (cf. Section V). This is in sharp contrast with the well behaved  $D_2$  and  $D_{2h}$  curves.

The stripy and zigzag order is typically identified by magnetic Bragg peaks at M points of the honeycomb Brillouin zone [29, 52, 53]. However, the  $D_2$  and  $D_{2h}$  order exhibit the same static structure factor (Figure 5), as the four orders share the same magnetic unit cell (Figure 1). Together with the explicit measurements of magnetizations and the agreement between our phase diagram Figure 2b with the previous numerical results [54], one can conclude that the optimal order parameters of the exotic states in HK model are given by  $D_2$  and  $D_{2h}$  matrices.

## V. HIDDEN SYMMETRIES

The  $D_2$  and  $D_{2h}$  ordering matrices in Table I are a finite set of orthogonal matrices, which preserve the spin length and are invertible. This means that, inverting the transformations, the exotic  $D_2$  and  $D_{2h}$  order can be converted to simple ferromagnets.

Specifically, one can define  $\tilde{S}$  using a sublattice-dependent coordinate,  $\tilde{S}_k = (T_k^{A,B})^T \tilde{S}$ . The magnetization Eq. (4) then becomes  $\tilde{M} = \tilde{M} = \sum_k \tilde{S}_k$ , describing a ferromagnetic alignment of  $\tilde{S}$ .

The above transformation acts on spin patterns. Naturally, one will examine the form of the Hamiltonian in the same coordinate system. Without loss of generality, we focus on the interaction of a local bond  $\langle kl \rangle_\gamma$ , which can be rewritten as

$$H_{kl} = \tilde{S}_k^T \hat{J}_\gamma \tilde{S}_l, \quad (5)$$

where  $\hat{J}_\gamma$  has three possibilities depending on the type of

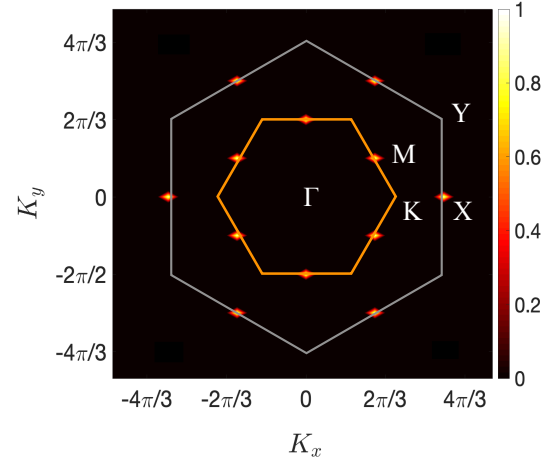


FIG. 5. Static structure factor for the stripy, zigzag,  $D_2$  and  $D_{2h}$  order. The four orders display the same momentum-space feature with magnetic Bragg peaks at M points, but are distinguished by the real-space order parameters given in Table I. The orange and grey hexagon denote the first and second honeycomb Brillouin zone, and high symmetry points are indicated. A nearest-neighbor bond of the honeycomb lattice is set to unit length.

the bond,

$$\begin{pmatrix} K+J & J \\ J & J \end{pmatrix}, \begin{pmatrix} J & K+J \\ J & J \end{pmatrix}, \begin{pmatrix} J & J \\ J & K+J \end{pmatrix}. \quad (6)$$

(Such expression can be easily generalized to other spin Hamiltonians.)

Under the sublattice-dependent coordinate transformations, Eq. (6) becomes

$$\tilde{H}_{kl} = \tilde{S}_k^T (\hat{T}_k^{A,B})^T \hat{J}_\gamma \hat{T}_k^{A,B} \tilde{S}_l. \quad (7)$$

The three different bonds transform as

$$\begin{aligned} \hat{J}_x &\rightarrow (\hat{T}_2^{A,B})^T \hat{J}_x \hat{T}_3^{A,B}, (\hat{T}_4^{A,B})^T \hat{J}_x \hat{T}_1^{A,B}; \\ \hat{J}_y &\rightarrow (\hat{T}_{3(1)}^{A(B)})^T \hat{J}_y \hat{T}_{1(3)}^{B(A)}, (\hat{T}_{4(2)}^{A(B)})^T \hat{J}_y \hat{T}_{2(4)}^{B(A)}; \\ \hat{J}_z &\rightarrow (\hat{T}_1^{A,B})^T \hat{J}_z \hat{T}_2^{A,B}, (\hat{T}_3^{A,B})^T \hat{J}_z \hat{T}_4^{A,B}; \end{aligned}$$

respectively leading to

$$\pm \begin{pmatrix} K+J & -J \\ -J & -J \end{pmatrix}, \pm \begin{pmatrix} -J & K+J \\ K+J & -J \end{pmatrix}, \pm \begin{pmatrix} -J & -J \\ -J & K+J \end{pmatrix}, \quad (8)$$

where “+” (“-”) corresponds to the  $D_2$  ( $D_{2h}$ ) order.

Clearly, at  $K = -2J$ , the couplings in the sublattice coordinate reduce to isotropic matrices,  $\pm J \mathbb{1}$ , where  $\mathbb{1}$  denotes the identity matrix.  $\tilde{H}_{kl}$  is simply the local interaction for a ferromagnetic Heisenberg model of spin  $\tilde{S}$ , with  $J > 0$  ( $< 0$ ) in the  $D_2$  ( $D_{2h}$ ) phase. This precisely reproduces the hidden  $O(3)$  symmetries of the HK model, which are previously identified in Ref. [31] by a dual transformation.

The above way of identifying hidden symmetries is especially straightforward. The high-symmetry points are self-evident once the order parameters are detected. It does not use specific properties and does hence not rely on prior insights of a Hamiltonian.

## VI. SUMMARY AND OUTLOOK

In summary, we demonstrated that TK-SVM provides a data-driven routine to search for hidden symmetries in exotic magnets. In comparison with other constructions, which are typically contingent on the skill and experience of the researcher, this approach does not require particular knowledge of the Hamiltonian and is feasible even when prior insights on the system are limited.

We considered the honeycomb Heisenberg-Kitaev model as an example and successfully identified its hidden  $O(3)$  points and their transformations. Moreover, we clarified that the full magnetization of exotic states in this model corresponds to a  $D_2$  and  $D_{2h}$  order (Figure 3). These results emphasize the significance of explicit order parameters to many-body spin systems, since the static structure factor does not encode all information of a magnetic phase. They also highlight the interpretability of a machine-learning method, as the machine results need to be decoded for physical understanding.

Exotic magnets realize one typical class of hidden symmetries. Below, we would like to outline possibilities of learning other types of hidden symmetries, though each of those merits systematic research.

In the case where a high-symmetry point is present at a critical point, rather than inside an ordered phase as is the case in the present paper, the hidden symmetry can in principle be global or local. In either case, it may induce emergent quantities reflecting that symmetry. TK-SVM is capable of detecting such quantities. Take the Kitaev limits ( $K = \pm 1, J = 0$ ) for example, which appear as critical points in the classical Heisenberg-Kitaev phase diagram (Figure 2b). We showed in Ref. [42] that TK-SVM manifested their local  $Z_2$  symmetries by probing the ground-state constraints of Kitaev spin liquids. We save the situations such as the global  $SU(3)$  symmetry in the bilinear-biquadratic chain for future work.

Hidden symmetries are also found in symmetry-protected topological states such as the hidden  $Z_2 \times Z_2$  symmetry in the celebrated Haldane phase [55–58]. The Haldane phase, as well as an array of other symmetry-protected topological states, can be mapped onto Landau-type orders by a nonlocal unitary transformation associated with the respective hidden symmetry [57–64]. However, how to detect such hidden symmetries with machine-learning techniques is not obvious in general owing to their topological nature [65–67]. Although it might be possible to construct an *ad hoc* machine for a particular SPT phase, devising an expressive machine that is applicable to a (reasonably wide) class of topological phases remains an open question.

## OPEN SOURCE AND DATA AVAILABILITY

The TK-SVM library has been made openly available with documentation and examples [68]. The data used in this work are available upon request.

## ACKNOWLEDGMENTS

We thank Philippe Corboz, Jheng-Wei Li, and Hong-Hao Tu for useful discussions. NR, KL, and LP acknowledge support from FP7/ERC Consolidator Grant QSIM-CORR, No. 771891, and the Deutsche Forschungsgemeinschaft (DFG, German Research Foundation) under Germany’s Excellence Strategy – EXC-2111 – 390814868. Our simulations make use of the  $\nu$ -SVM formulation [69], the LIBSVM library [70, 71], and the ALPSCore library [72].

## Appendix A: Setting up of TK-SVM

Here we provide more details of TK-SVM and refer the reader to Refs. [39, 40] for the introduction of the method and Ref. [41] for a review, including comprehensive discussions on how to interpret  $C_{\mu\nu}$  matrices.

The map  $\phi$  in the decision function Eq. (2) maps a spin sample  $\mathbf{x}$  to a configuration of degree  $n$  monomials,

$$\phi : \mathbf{x} \rightarrow \phi(\mathbf{x}) = \{\phi_\mu\} = \{\langle S_{a_1}^{\alpha_1} \dots S_{a_n}^{\alpha_n} \rangle_{cl}\}, \quad (A1)$$

where  $n$  also corresponds to the rank of a TK-SVM. This mapping partitions the system into clusters containing  $r$  spins labelled with  $\alpha_n = \{1, 2 \dots r\}$ , while  $\mu = \{\alpha_n, a_n\} = \{\alpha_1, a_1, \dots, \alpha_n, a_n\}$  denotes a collective index.  $\phi$  is then averaged over the clusters, indicated by  $\langle \dots \rangle_{cl}$ , to reduce the dimension of the data. The optimal choice for the size and shape of the clusters is in general unknown *a priori*, and different phases in a phase diagram may have distinct translational symmetries. Therefore, in practice, we adopt clusters comprising a large number of lattice unit cells in order to accommodate diverse orders. In the results presented in the current work, clusters with a size up to 288 spins ( $12 \times 12$  honeycomb unit cells) were used.

The  $C_{\mu\nu}$  matrix is defined by a weighted sum over support vectors,

$$C_{\mu\nu} = \sum_k \lambda_k \phi_\mu(\mathbf{x}^{(k)}) \phi_\nu(\mathbf{x}^{(k)}), \quad (A2)$$

where  $\lambda_k$  is a Lagrange multiplier solved in the underlying SVM optimization problem,  $\lambda_k \neq 0$  corresponds to a support vector. Non-vanishing entries of  $C_{\mu\nu}$  represent correlations between particular monomial components.

Figure 6 shows the  $C_{\mu\nu}$  of the  $D_2$  and  $D_{2h}$  order for example. Their interpretation gives rise to the ordering matrices in Table I.

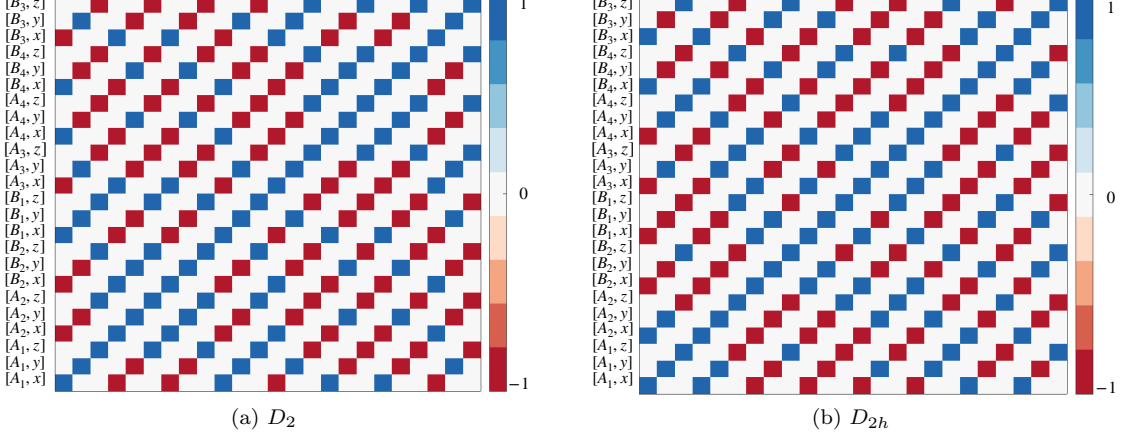


FIG. 6. The  $C_{\mu\nu}$  matrices learned by a rank-1 TK-SVM for the  $D_2$  and  $D_{2h}$  orders. Each pixel represents a correlation between two spin components defined by the weighted sum of the support vectors in Eq. (A2). Here an eight-spin cluster ( $2 \times 2$  honeycomb unit cells), which is the minimal translational unit for the  $D_2$  and  $D_{2h}$  order, is used for demonstration. From bottom to top, the vertical axis is labeled in the same convention as in the lattice Figure 1. The same labeling applies to the horizontal axis from left to right. The interpretation of these patterns lead to the respective ordering matrices in Table I.

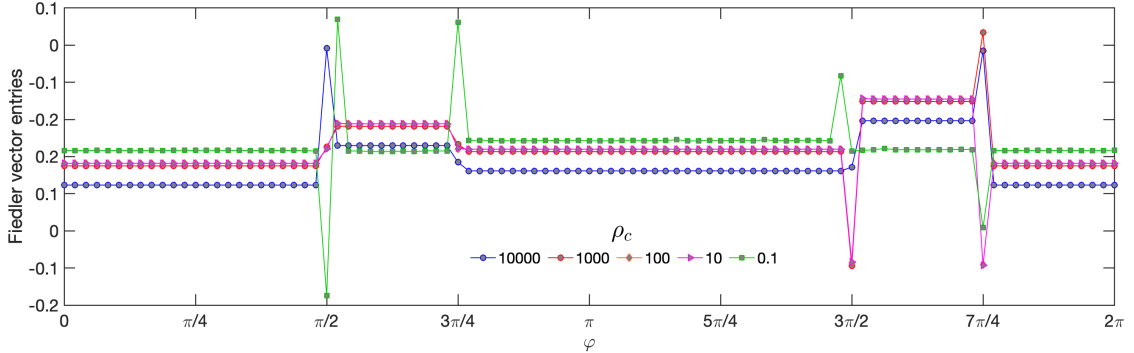


FIG. 7. Fiedler vectors obtained with different choices of  $\rho_c$ . Contrasts between Fiedler-vector entries, rather than the values themselves, reflect the partitioning, namely, the topology of the phase diagram. In all cases, where  $\rho_c$  is large enough to set a characteristic scale “ $\gg 1$ ” for the reduced  $\rho$  criterion Eq. (B1), the clustering is evident and robust. The profound jumps at  $\varphi = \frac{\pi}{2}, \frac{3\pi}{4}, \frac{3\pi}{2}, \frac{7\pi}{4}$  correspond to phase boundaries, as they do not belong to any plateaus (stable phases). A case of small  $\rho_c = 0.1$  is also included for comparison.  $\rho_c = 100$  is used in the maintext.

## Appendix B: Details of Graph Partitioning

For a binary classification between two sample sets “A” and “B”, the parameter  $\rho$  in decision function Eq. (2) behaves as

$$|\rho_{AB}| \begin{cases} \gg 1 & \text{A, B in the same phase,} \\ \lesssim 1 & \text{A, B in different phases,} \end{cases} \quad (\text{B1})$$

which is referred as the reduced  $\rho$  criterion [40, 41].

The weight of an edge in the graph Figure 2a is determined by  $\rho$  in the decision function learned for the two end points, with a Lorentzian weighting function,

$$w(\rho) = 1 - \frac{\rho^2}{(|\rho| - 1)^2 + \rho_c^2} \in [0, 1], \quad (\text{B2})$$

where  $\rho_c$  is a super-parameter introduced to set a characteristic scale for “ $\gg 1$ ” in the above reduced  $\rho$  criterion. However, as we will discuss in Figure 7, the choice of  $\rho_c$  is not crucial.

The graph Figure 2a can be described by a Laplacian matrix,

$$\hat{L} = \hat{D} - \hat{A} = \begin{bmatrix} d_1 & -w_{12} & \dots & -w_{1M} \\ -w_{21} & d_2 & \dots & -w_{2M} \\ \vdots & & & \vdots \\ -w_{M1} & -w_{M2} & \dots & d_M \end{bmatrix}. \quad (\text{B3})$$

Here, the off-diagonal entries,  $\omega_{ij} = \omega_{ji} = \omega(\rho_{ij})$ , host all the edge weights and are collected by the adjacency matrix  $\hat{A}$ . The diagonal entries,  $d_i = \sum_{j \neq i} \omega(\rho_{ij})$ , represent degrees of the vertices and form the degree matrix  $\hat{D}$ .  $\hat{L}$  is symmetric by construction as only the magnitude of  $\rho$

is used. (The sign of  $\rho$  can reveal which data set is more disordered, but this property is not needed for the graph partitioning; see Refs. [40] and [41] for details.) According to Fiedler's theory [43, 44], partitioning of a graph can be formulated as an eigenproblem of  $\hat{L}$ , as shown in Eq. (3). The second smallest eigenvector, known as the Fiedler vector, reflects the clustering of the graph.

In Figure 7, we compare the resultant Fiedler vectors

using different values of  $\rho_c$ . The  $M$  vertices are classified into distinct subgraph components (indicated by the plateaus). In the case of  $\rho_c = 0.1$ , which does not suffice to define a scale “ $\gg 1$ ”, the partitioning is less obvious as all Fiedler-vector entries display very similar values. However, in all other cases, where  $\rho_c$  crosses several orders, the clustering is clear and robust.

---

[1] G. Carleo, I. Cirac, K. Cranmer, L. Daudet, M. Schuld, N. Tishby, L. Vogt-Maranto, and L. Zdeborová, *Rev. Mod. Phys.* **91**, 045002 (2019).

[2] L. Zdeborov and F. Krzakala, *Advances in Physics* **65**, 453 (2016).

[3] J. Sohl-Dickstein, E. A. Weiss, N. Maheswaranathan, and S. Ganguli, arXiv preprint arXiv:1503.03585 (2015).

[4] G. Carleo and M. Troyer, *Science* **355**, 602 (2017).

[5] L. Wang, *Phys. Rev. B* **94**, 195105 (2016).

[6] J. Carrasquilla and R. G. Melko, *Nat. Phys.* **13**, 431 (2017).

[7] Z. Nussinov, P. Ronhovde, D. Hu, S. Chakrabarty, B. Sun, N. A. Mauro, and K. K. Sahu, “Inference of hidden structures in complex physical systems by multi-scale clustering,” in *Information Science for Materials Discovery and Design*, edited by T. Lookman, F. J. Alexander, and K. Rajan (Springer International Publishing, Cham, 2016) pp. 115–138.

[8] K. T. Butler, D. W. Davies, H. Cartwright, O. Isayev, and A. Walsh, *Nature* **559**, 547 (2018).

[9] D. Morgan and R. Jacobs, *Annual Review of Materials Research* **50**, null (2020).

[10] D. Guest, K. Cranmer, and D. Whiteson, *Annual Review of Nuclear and Particle Science* **68**, 161 (2018).

[11] A. Radovic, M. Williams, D. Rousseau, M. Kagan, D. Bonacorsi, A. Himmel, A. Aurisano, K. Terao, and T. Wongjirad, *Nature* **560**, 41 (2018).

[12] M. Ntampaka, C. Avestruz, S. Boada, J. Caldeira, J. Cisewski-Kehe, R. Di Stefano, C. Dvorkin, A. E. Evrard, A. Farahi, D. Finkbeiner, *et al.*, arXiv preprint arXiv:1902.10159 (2019).

[13] M. Schuld and F. Petruccione, *Supervised Learning with Quantum Computers*, 1st ed. (Springer Publishing Company, Incorporated, 2018).

[14] J. Biamonte, P. Wittek, N. Pancotti, P. Rebentrost, N. Wiebe, and S. Lloyd, *Nature* **549**, 195 (2017).

[15] J. Haah, A. W. Harrow, Z. Ji, X. Wu, and N. Yu, *IEEE Transactions on Information Theory* **63**, 5628 (2017).

[16] D. Luo and B. K. Clark, *Phys. Rev. Lett.* **122**, 226401 (2019).

[17] D. Pfau, J. S. Spencer, A. G. d. G. Matthews, and W. M. C. Foulkes, arXiv preprint arXiv:1909.02487 (2019).

[18] J. Hermann, Z. Schätzle, and F. Noé, arXiv preprint arXiv:1909.08423 (2019).

[19] H.-J. Liao, J.-G. Liu, L. Wang, and T. Xiang, *Phys. Rev. X* **9**, 031041 (2019).

[20] G. Carleo, K. Choo, D. Hofmann, J. E. Smith, T. Westerhout, F. Alet, E. J. Davis, S. Efthymiou, I. Glasser, S.-H. Lin, M. Mauri, G. Mazzola, C. B. Mendl, E. [van Nieuwenburg], O. O'Reilly, H. Thveniaut, G. Torlai, F. Vicentini, and A. Wietek, *SoftwareX* **10**, 100311 (2019).

[21] Y. Nagai, H. Shen, Y. Qi, J. Liu, and L. Fu, *Phys. Rev. B* **96**, 161102 (2017).

[22] Y. Zhang, A. Mesaros, K. Fujita, S. D. Edkins, M. H. Hamidian, K. Ch'ng, H. Eisaki, S. Uchida, J. C. S. Davis, E. Khatami, and E.-A. Kim, *Nature* **570**, 484 (2019).

[23] G. Torlai, B. Timar, E. P. L. van Nieuwenburg, H. Levine, A. Omran, A. Keesling, H. Bernien, M. Greiner, V. Vuletić, M. D. Lukin, R. G. Melko, and M. Endres, *Phys. Rev. Lett.* **123**, 230504 (2019).

[24] A. Bohrdt, C. S. Chiu, G. Ji, M. Xu, D. Greif, M. Greiner, E. Demler, F. Grusdt, and M. Knap, *Nature Physics* **15**, 921 (2019).

[25] A. Kitaev, *Ann. Phys. (N. Y.)* **321**, 2 (2006), january Special Issue.

[26] G. Jackeli and G. Khaliullin, *Phys. Rev. Lett.* **102**, 017205 (2009).

[27] J. Chaloupka, G. Jackeli, and G. Khaliullin, *Phys. Rev. Lett.* **105**, 027204 (2010).

[28] H. Takagi, T. Takayama, G. Jackeli, G. Khaliullin, and S. E. Nagler, *Nat. Rev. Phys.* **1**, 264 (2019).

[29] L. Janssen and M. Vojta, *J. Phys.: Condens. Matter* **31**, 423002 (2019).

[30] S. M. Winter, A. A. Tsirlin, M. Daghofer, J. van den Brink, Y. Singh, P. Gegenwart, and R. Valentí, *Journal of Physics: Condensed Matter* **29**, 493002 (2017).

[31] J. Chaloupka and G. Khaliullin, *Phys. Rev. B* **92**, 024413 (2015).

[32] J. Chaloupka, G. Jackeli, and G. Khaliullin, *Phys. Rev. Lett.* **110**, 097204 (2013).

[33] J. Rusnáčko, D. Gotfrýd, and J. Chaloupka, *Phys. Rev. B* **99**, 064425 (2019).

[34] G. Uimin, *JETPL* **12**, 225 (1970).

[35] C. K. Lai, *Journal of Mathematical Physics* **15**, 1675 (1974).

[36] B. Sutherland, *Phys. Rev. B* **12**, 3795 (1975).

[37] C. D. Batista, G. Ortiz, and J. E. Gubernatis, *Phys. Rev. B* **65**, 180402 (2002).

[38] B. Zhao, P. Weinberg, and A. W. Sandvik, *Nature Physics* **15**, 678 (2019).

[39] J. Greitemann, K. Liu, and L. Pollet, *Phys. Rev. B* **99**, 060404(R) (2019).

[40] K. Liu, J. Greitemann, and L. Pollet, *Phys. Rev. B* **99**, 104410 (2019).

[41] J. Greitemann, K. Liu, L. D. C. Jaubert, H. Yan, N. Shannon, and L. Pollet, *Phys. Rev. B* **100**, 174408 (2019).

[42] K. Liu, N. Sadoune, N. Rao, J. Greitemann, and L. Pollet, arXiv preprint arXiv:2004.14415 (2020).

[43] M. Fiedler, Czechoslovak Mathematical Journal **23**, 298 (1973).

[44] M. Fiedler, Czechoslovak Mathematical Journal **25**, 619 (1975).

[45] L. Janssen, E. C. Andrade, and M. Vojta, Phys. Rev. Lett. **117**, 277202 (2016).

[46] J. Osorio Iregui, P. Corboz, and M. Troyer, Phys. Rev. B **90**, 195102 (2014).

[47] M. Gohlke, R. Verresen, R. Moessner, and F. Pollmann, Phys. Rev. Lett. **119**, 157203 (2017).

[48] J. Wang, B. Normand, and Z.-X. Liu, Phys. Rev. Lett. **123**, 197201 (2019).

[49] X.-Y. Dong and D. Sheng, arXiv preprint arXiv:1911.12854 (2019).

[50] G. Khaliullin and S. Okamoto, Phys. Rev. Lett. **89**, 167201 (2002).

[51] G. Khaliullin, Progress of Theoretical Physics Supplement **160**, 155 (2005).

[52] A. Banerjee, C. A. Bridges, J. Q. Yan, A. A. Aczel, L. Li, M. B. Stone, G. E. Granroth, M. D. Lumsden, Y. Yiu, J. Knolle, S. Bhattacharjee, D. L. Kovrizhin, R. Moessner, D. A. Tennant, D. G. Mandrus, and S. E. Nagler, Nat. Mater. **15**, 733 (2016).

[53] A. Banerjee, J. Yan, J. Knolle, C. A. Bridges, M. B. Stone, M. D. Lumsden, D. G. Mandrus, D. A. Tennant, R. Moessner, and S. E. Nagler, Science **356**, 1055 (2017).

[54] L. Janssen, E. C. Andrade, and M. Vojta, Phys. Rev. B **96**, 064430 (2017).

[55] I. Affleck, T. Kennedy, E. H. Lieb, and H. Tasaki, Phys. Rev. Lett. **59**, 799 (1987).

[56] I. Affleck, T. Kennedy, E. H. Lieb, and H. Tasaki, Communications in Mathematical Physics **115**, 477 (1988).

[57] T. Kennedy and H. Tasaki, Phys. Rev. B **45**, 304 (1992).

[58] T. Kennedy and H. Tasaki, Communications in Mathematical Physics **147**, 431 (1992).

[59] M. den Nijs and K. Rommelse, Phys. Rev. B **40**, 4709 (1989).

[60] H.-H. Tu, G.-M. Zhang, and T. Xiang, Phys. Rev. B **78**, 094404 (2008).

[61] H.-H. Tu, G.-M. Zhang, and T. Xiang, Journal of Physics A: Mathematical and Theoretical **41**, 415201 (2008).

[62] H.-H. Tu, G.-M. Zhang, T. Xiang, Z.-X. Liu, and T.-K. Ng, Phys. Rev. B **80**, 014401 (2009).

[63] D. V. Else, S. D. Bartlett, and A. C. Doherty, Phys. Rev. B **88**, 085114 (2013).

[64] K. Duivenvoorden and T. Quella, Phys. Rev. B **88**, 125115 (2013).

[65] Z.-C. Gu and X.-G. Wen, Phys. Rev. B **80**, 155131 (2009).

[66] X. Chen, Z.-C. Gu, and X.-G. Wen, Phys. Rev. B **83**, 035107 (2011).

[67] F. Pollmann, E. Berg, A. M. Turner, and M. Oshikawa, Phys. Rev. B **85**, 075125 (2012).

[68] J. Greitemann, K. Liu, and L. Pollet, tensorial-kernel SVM library, <https://gitlab.physik.uni-muenchen.de/tk-svm/tksvm-op>.

[69] B. Schölkopf, A. J. Smola, R. C. Williamson, and P. L. Bartlett, Neural Comput. **12**, 1207 (2000).

[70] C.-C. Chang and C.-J. Lin, Neural Comput. **13**, 2119 (2001).

[71] C.-C. Chang and C.-J. Lin, ACM Trans. Intell. Syst. Technol. **2**, 27:1 (2011).

[72] A. Gaenko, A. Antipov, G. Carcassi, T. Chen, X. Chen, Q. Dong, L. Gamper, J. Gukelberger, R. Igarashi, S. Iskakov, M. Könz, J. LeBlanc, R. Levy, P. Ma, J. Paki, H. Shinaoka, S. Todo, M. Troyer, and E. Gull, Comput. Phys. Commun. **213**, 235 (2017).